Pergamon

Int. J. Heat Mass Transfer. Vol. 37, No. 7, pp. 1101–1109, 1994

0017–9310/94 $6.00 + 0.00

0017–9310(93)E0030–K

Bifurcation phenomenon during the fixed-solid-mode melting inside a horizontal cylinder

SUNG TACK RO and CHARN-JUNG KIM

Department of Mechanical Engineering, Seoul National University, Seoul 151-742, Korea

(*Received* 14 *July* 1993 *and in final form* 27 *October* 1993)

Abstract—As for the inward melting inside an isothermal horizontal cylinder, where the unmelted solid core is constrained from moving under gravity, two drastically different melting patterns have been reported in the literature; the shape of the melting surface in the bottom portion has been observed to be either concave or convex. The present work was motivated to elucidate the main cause of these conflicting results. This was done first by obtaining the full transient solutions conforming to the model equations, and then by introducing the bifurcation times as well as a pair of bifurcating solutions. It was found that the convex pear-like melting surface could be well explained in terms of the primary bifurcating solution. Another mode of melting, in which the concave crater shape of the melting surface was observed, turned out to be also a kind of branching solution to the melting process of interest.

INTRODUCTION

CONVECTION-DOMINATED melting problems have been extensively studied in various geometric arrangements. For instance, melting inside an isothermal horizontal cylinder has received much attention as a model of the latent heat-of-fusion storage system. In particular, the inward melting process in which the unmelted solid core is constrained from moving under gravity has been studied in a number of publications [1–3]. However, these studies produced drastically different melting patterns, especially for the shape of the melting surface in the bottom portion. Saitoh and Hirose [1] observed experimentally the development of a concave bottom surface, whereas Rieger *et al.* [2] as well as Ho and Viskanta [3] observed a convex pear-like melting surface for moderate to high Rayleigh numbers. The numerical simulations from these studies were also strikingly different from one another. Despite these results and those of subsequent investigations [4, 5], no convincing explanation has been offered so far for the conflicting results between different investigations on an identical problem. The main cause of this discrepancy has been vaguely attributed to the highly unstable flow circulation present in the bottom portion.

It has been widely known in the literature that the solution of the nonlinear Navier–Stokes differential systems is not necessarily unique. Such a peculiar situation occurs when the thermal instability plays a vital role of determining the flow structure, e.g. two-dimensional steady-state natural convection in a horizontal annulus [6, 7]. The multiplicity of solutions is related to bifurcation phenomena, and has been confirmed both numerically [7–10] and experimentally [11, 12].

In recognition of the bifurcation phenomenon associated with natural convection problems, Park and Chang [13] suggested that the aforementioned conflicting results might be caused by the existence of bifurcating solutions. In order to create such dual solutions in their enthalpy formulation, they applied a small perturbation to the vorticity field when the melt gap reached 3% of the tube diameter, and then obtained two families of branching solutions at a high Rayleigh number; the flow pattern of one branching solution was bicellular, and the other was tricellular. Nevertheless, their analysis could not explain the experimental observation [3] that as melting continued the multi-cells began to merge together at moderate melting stage and subsequently the unicellular flow pattern became predominant for the rest of melting stages. In fact, the pear-shaped solid core which was observed in the experiments [2, 3] was a direct consequence of the life and death of a pair of secondary vortices in the bottom portion.

In the present study, we presented two families of bifurcating solutions to the inward melting process, in addition to the numerical solutions that were obtained directly from the model equations and boundary conditions. Both the bifurcating solutions were found to qualitatively agree well with the available experimental results. Several important conclusions are drawn here that the conventional model equations for the melting process may lead to somehow anti-physical solution, and that two conflicting melting patterns are all physically possible and imparted by the multiplicity of solutions.

ANALYSIS

Model equations and boundary conditions

A schematic of the physical model for melting inside a horizontal cylinder of radius R_w is presented in Fig. 1. The cylinder is initially filled with subcooled solid

NOMENCLATURE

c	specific heat
h	specific enthalpy
h_{sf}	latent heat of fusion
h_ξ, h_η	geometric factors
J	Jacobian
m_f	melt volume fraction
$\overline{Nu}$	average Nusselt number
p	pressure
Pr	Prandtl number
R	radial coordinate
R_f	radial position of solid–liquid interface
R_w	radius of cylinder
Ra	representative Rayleigh number, $g\beta(T_w-T_f)R_w^3/(\nu\alpha_L)$
Ra_δ	effective Rayleigh number based on the melt gap width
S_C	subcooling number, $c_S(T_f-T_0)/h_{sf}$
Ste	Stefan number, $c_L(T_w-T_f)/h_{sf}$
t	time
T_0	initial temperature of solid
T_f	melting temperature
T_w	wall temperature
u, v	Cartesian velocity components
x, y	Cartesian coordinates
x_t, y_t	mesh velocities.

Greek symbols

α	thermal diffusivity
α_ξ, α_η	geometric factors
β_ξ, β_η	geometric factors
Γ	exchange coefficient
θ	dimensionless enthalpy
Θ	angular coordinate
ν	kinematic viscosity
ξ, η	transformed coordinates
ρ	density
τ	dimensionless time, $Ste\,Fo$, $Fo=\alpha_L t/R_w^2$
ϕ	general dependent variable.

Superscript

+	dimensionless.

Subscripts

f	interface
L	liquid
r	solid-to-liquid property ratio
S	solid
t–u	tricellular-to-unicellular transition
u–b	unicellular-to-bicellular transition
w	cylinder wall.

(at a uniform temperature T_0). At time $t=0$, the temperature of the cylinder wall is suddenly raised to a fixed value of $T_w > T_f$ and melting occurs instantaneously. At early times conduction is the primary mode of heat transfer and, therefore, the melting surface proceeds concentrically. Later, as natural convection develops and intensifies in the liquid, the solid–liquid interface is exposed to a nonuniform heat transfer rate and consequently begins to deviate from its initial concentric shape, as illustrated in Fig. 1.

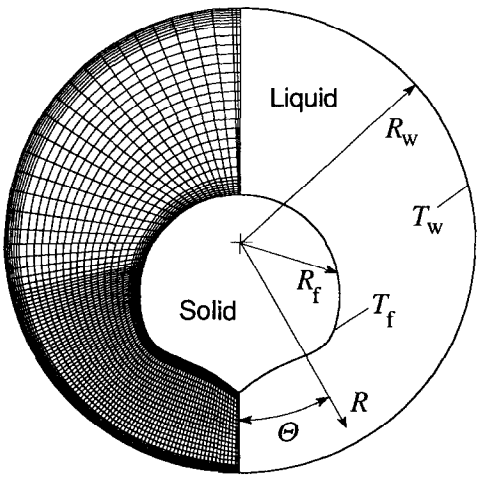

FIG. 1. Schematic diagram of the inward melting process in a horizontal cyinder and a grid system of 31 × 105 resolution constructed in the liquid.

Several simplifications are employed for the analysis: the melting process is two-dimensional and symmetric with respect to the vertical diameter; the unmelted solid core is fixed in space; the density change between the phases is negligible; the liquid is Newtonian and the flow is laminar; the thermophysical properties are constant except for the variation of density with temperature (the Boussinesq approximation). These have been accepted as reasonable first-order approximations [1–3].

The initial subcooling of solid is also taken into account in this study. Accordingly, the relevant field variables in both the liquid and solid phases need to be resolved in conjunction with the constraints specified at the solid–liquid interface. To facilitate our analysis, we consider the general conservation equation written as

$$\frac{\partial}{\partial t}(\rho\phi)+\frac{\partial}{\partial x}\left(\rho u\phi-\Gamma\frac{\partial\phi}{\partial x}\right)+\frac{\partial}{\partial y}\left(\rho v\phi-\Gamma\frac{\partial\phi}{\partial y}\right)=S(x,y). \quad (1)$$

The above equation is repeated for the continuity, momentum, and energy equations for the liquid phase; and the energy equation for the solid phase.

Table 1. Variables in the dimensionless conservation equation. The length, time, velocity, pressure and specific enthalpies† are scaled with R_w, R_w^2/α_L, α_L/R_w, $\rho_L\alpha_L^2/R_w^2$ and $c_L(T_w-T_f)$, respectively. Here, $Pr = 53.84$ and $\alpha_r = 2.876$ are used for computation

	ϕ^+	Γ^+	S^+
Solid	θ_S	α_r	0
Liquid	1	0	0
	u^+	Pr	$-\partial p^+/\partial x^+$
	v^+	Pr	$-\partial p^+/\partial y^+ + Ra\,Pr\,\theta_L$
	θ_L	1	0

† $h_L = c_L(T_L-T_f)+h_{sf}$, $h_S = c_S(T_S-T_f)$.

The complete set of governing equations is then rendered dimensionless and summarized in Table 1.

The treatment of the moving interface is effected via the boundary immobilization techniques. Accordingly, a transformed (ξ, η) coordinate

$$x = x(\xi, \eta, t), \quad y = y(\xi, \eta, t) \tag{2}$$

is introduced such that the moving interface can be immobilized particularly at a constant ξ-line. Then, equation (1) can be transformed into

$$\frac{\partial}{\partial t}(J\rho\phi) + \frac{\partial}{\partial \xi}\left(\rho U\phi - \frac{\alpha_\xi \Gamma}{h_\xi}\frac{\partial \phi}{\partial \xi}\right) + \frac{\partial}{\partial \eta}\left(\rho V\phi - \frac{\alpha_\eta \Gamma}{h_\eta}\frac{\partial \phi}{\partial \eta}\right) = JS(\xi,\eta) - \frac{\partial}{\partial \xi}\left(\frac{\beta_\xi \Gamma}{h_\eta}\frac{\partial \phi}{\partial \eta}\right) - \frac{\partial}{\partial \eta}\left(\frac{\beta_\eta \Gamma}{h_\xi}\frac{\partial \phi}{\partial \xi}\right) \tag{3}$$

where

$$U = \alpha_\xi u_\xi - \beta_\xi u_\eta - X_t, \quad V = \alpha_\eta u_\eta - \beta_\eta u_\xi - Y_t$$
$$X_t = y_\eta x_t - x_\eta y_t, \quad Y_t = x_\xi y_t - y_\xi x_t$$
$$u_\xi = (x_\xi u + y_\xi v)/h_\xi, \quad U_\eta = (x_\eta u + y_\eta v)/h_\eta. \tag{4}$$

Other factors appearing in equations (3) and (4) are available in ref. [14].

The boundary conditions at the solid–liquid interface are the constraint of motionless solid, the continuity of temperature, and the conservation of the mass and energy fluxes, i.e.

$$u = v = 0 \tag{5}$$

$$T_L = T_S = T_f \tag{6}$$

$$(\rho U)_L = (\rho U)_S \tag{7}$$

$$\left(\rho Uh - \frac{\alpha_\xi \Gamma}{h_\xi}\frac{\partial h}{\partial \xi}\right)_L = \left(\rho Uh - \frac{\alpha_\xi \Gamma}{h_\xi}\frac{\partial h}{\partial \xi}\right)_S. \tag{8}$$

The additional boundary conditions for the temperature and velocity fields are

$$\text{cylinder wall:} \quad T_L = T_w, \quad u = v = 0 \tag{9}$$

$$\text{line of symmetry:} \quad \frac{\partial T}{\partial x} = 0, \quad u = 0, \quad \frac{\partial v}{\partial x} = 0 \tag{10}$$

Solution procedure

In order to highly utilize the geometric configuration shown in Fig. 1, the polar coordinate was selected as a subsidiary system:

$$x = R\sin\Theta, \quad y = -R\cos\theta \tag{11}$$

where

$$R = \begin{cases} R_f\xi & \text{for } 0 \leqslant \xi < 1 \\ R_f + (\xi-1)(R_w - R_f) & \text{for } 1 \leqslant \xi \leqslant 2 \end{cases} \tag{12}$$

$$\Theta = \eta \quad \text{for} \quad 0 \leqslant \eta \leqslant \pi. \tag{13}$$

It should be noted that this polar coordinate does not participate in the discretization procedure but is used only in deploying the computational control volumes. In the transformed (ξ, η) coordinate, the moving interface is immobilized at $\xi = 1$ for all times.

A nonuniform grid system of 31×105 resolution was selected in each phase and used for computation. In the left-half of Fig. 1, the grid system constructed in the liquid domain is illustrated. As shown there, computational cells are densely spaced along the bottom portion and near the walls, expecting large gradients of field variables to occur in those regions. The selection of such a refined grid system was based on the fact that the number of nodes in the angular direction was of great importance in simulating the bifurcation phenomenon [7].

The discretization procedure followed in this study has been well documented elsewhere [14], thus obviating detailed explanation. Specifically, the mesh velocities arising from the coordinate transformation were treated in accord with the area rule [14, 15] so as to satisfy the global mass conservation. To avoid the initial singularity, a thin liquid layer of uniform thickness $0.01R_w$ was assumed to exist and computation commenced thereafter. The interface movement was treated explicitly and controlled by using a variable time step. Further details on the interface-identifying procedure can be found in refs. [14–16]. Especially, due to an explicit treatment of interface movement, the time increment per each marching was required to be chosen properly. For this reason, the balance between the net change in the stored energy and the total amount of heat passed through the wall was checked at each time step. It was found that when the maximum changes in phase thicknesses over each time interval were monitored to be less than 0.3% the energy conservation was satisfied to within 0.05%.

RESULTS AND DISCUSSION

Preliminary results: the full transient solution

The previous analytical results [1–3] on the inward melting in a horizontal cylinder are all based on an identical set of governing equations and boundary

Table 2. The numerical approaches adopted in the earlier studies and in the present study

References	Grid resolution	Basic formulation	Quasi-steady assumption	Shape of the solid core
Saitoh and Hirose [1]	18×14	Stream function–vorticity	Yes	Concave
Reiger *et al.* [2]	21×31	Stream function–vorticity	No	Convex
Ho and Viskanta [3]	13×21	Stream function–vorticity	Yes	Convex
This work†	31×105	Primitive variable	No	Convex

† Full transient solution.

conditions, as are repeated herein. Nevertheless, the numerical predictions from the earlier investigations are substantially different from one another, as far as the melting pattern in the bottom portion is concerned. Motivated by this, we decided first to examine the influence of the grid resolution on the melting pattern. As a preliminary step, Table 2 presents a brief comparison of the numerical approaches between the existing studies and this work. It is noteworthy that the quasi-steady assumptions have been employed in refs. [1, 3], i.e. a sequence of steady-state natural convection in the melt is determined over a number of quasi-static periods of time, during which the interface remains fixed [3]. The quasi-steady assumptions, although widely used in the analysis of melting problems, would invoke an ambiguity if a multiple number of steady-state solutions exist.

Disregarding the different grid resolutions, our numerical approach seems to be closer to that of Rieger *et al.* [2] in a sense that all the transient terms and the mesh velocities are included in the computation. In this respect, the numerical solution conforming to the aforementioned model equations will be referred to as the *full transient solution* hereinafter.

As an illustration of the full transient solution corresponding to a high Ra number, Fig. 2 exposes the distribution of streamlines and isotherms at an instant of time. It is evident that a pair of secondary counter-rotating cells coexist with a major recirculating flow in the melt. Although not shown in Fig. 2, our full transient solution revealed that the flow pattern was initially unicellular (due to the conduction domination at early melting) and subsequently transited to tricellular. The tricellular flow pattern shown in Fig. 2 was found to persist up to near complete melting. It

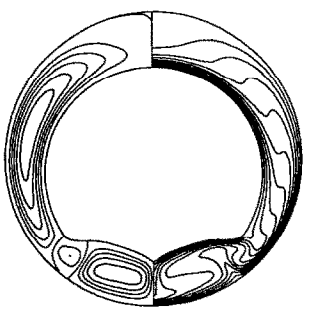

FIG. 2. The full transient solution at $\tau = 0.029$ for the case of $Ra = 1.2 \times 10^6$, $Ste = 0.133$ and $S_C = 0.004$.

can be recognized that our full transient solution is qualitatively similar to that from Rieger *et al.* [2], but still disagrees with the experimental observation of Ho and Viskanta [3] in which the transition from tricellular to unicellular pattern was detected at a moderate melting stage. However, the multicellular flow pattern has not been numerically predicted in Ho and Viskanta [3], due probably to the coarse grid system used (see Table 2).

By re-examining the melting process for a high Ra case with a refined grid system, the following conclusions are drawn.

- The use of a coarse grid system prevents the multicellular flow pattern from being predicted.
- The tricellular flow pattern of the full transient solution prevails over most of the melting process, except short periods of the initial and final stages of melting.
- No matter how dense the grid system may be, the full transient solution would fail to simulate the tricellular-to-unicellular transition at moderate melting stage, which has indeed been observed experimentally [3].

At this point, it is suspected that the foregoing model equations and boundary conditions are too much idealized to account for the potential instabilities associated with the natural convective heat transfer considered here.

Multiplicity of steady-state solutions

A wide variety of experimental or numerical evidences are available in the literature that indicate a multiplicity of solutions to natural convection problems. For example, Rao *et al.* [8] demonstrated that the bifurcating solutions to the natural convection in a porous annulus yielded better agreement with the reported experimental data. For spherical concentric annuli, Caltagirone *et al.* [9] show that the inner-heated case is mathematically equivalent to the inner-cooled one. In fact, the melting process considered here bears a close resemblance with the natural convection in an inner-cooled annulus.

In what follows, the possibility of a multiplicity of steady-state natural convection solutions is examined in connection with our full transient solutions. For this purpose, a large number of steady-state runs are made for a fixed Ra and for a series of geometric configurations that are recorded from the full tran-

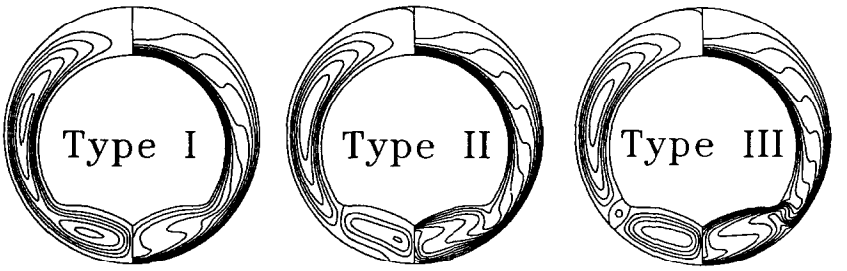

FIG. 3. The supplementary steady-state branching solutions corresponding to the same Rayleigh number and geometry as in Fig. 2.

sient solutions (with an interval of $\Delta\tau = 0.001$). It is well known in the bifurcation literature that the initial guesses play a decisive role of determining which of branches the converged solution is led to. Therefore, three different types of the initial guesses were tried to obtain steady-state solutions in the following manner.

- Type I: linear temperature profile in the ξ-direction and a stagnant flow.
- Type II: temperature field including an upward velocity in the lower symmetry line (i.e. at $\Theta = 0$), being an analogous approach to that used in ref. [7].
- Type III: temperature and velocity distributions from the full transient solution, which is no more than the quasi-steady assumption mentioned earlier.

Figure 3 displays three different modes of the steady-state solutions corresponding to the case where the geometry and the Rayleigh number are the same as in Fig. 2. As expected, the steady-state solution from Type III appears very similar to the full transient solution in Fig. 2.

The occurrence of a multiplicity of steady-state solutions, as shown in Fig. 3, relies strongly on the gap size between the interface and the wall. This is because the effective Rayleigh number based on the gap width (say Ra_δ) has a dominant influence on the flow bifurcation. For the present problem, the gap width (thus the effective Rayleigh number) varies with time. Therefore, we consider here the critical time (instead of the critical Ra_δ) after which two or more steady-state solutions come into existence. The procedure followed in this study is explained with the aid of Fig. 4 where the thicker line represents the path traced by the full transient solution. Within this schematic diagram, the three different branching solutions shown in Fig. 3 can be conveniently denoted by the hatched circles on dotted lines. The converged steady-state solutions at hatched circles were first used as the initial guesses to determine new steady-state solutions corresponding to the hatched squares (i.e. lower Ra_δ case). Moving left little by little in this way, the first bifurcation point was found at point D. This means that both the initial guesses of Types I and III, after final convergence, end up with the same tricellular flow pattern. In a similar way, the second bifurcation point was also found, as designated by point B in Fig. 4. Several features in Fig. 4 are addressed below.

- Only unicellular steady-state flows can exist below point B because the effective Rayleigh number Ra_δ is too low to allow for any thermal instability.
- The bicellular steady-state solution precedes the tricellular one. Apart from the different medium and geometric configuration considered, Rao *et al.* [8] also reported that as Ra_δ increased the bicellular flow was first observed and then the tricellular flow started to

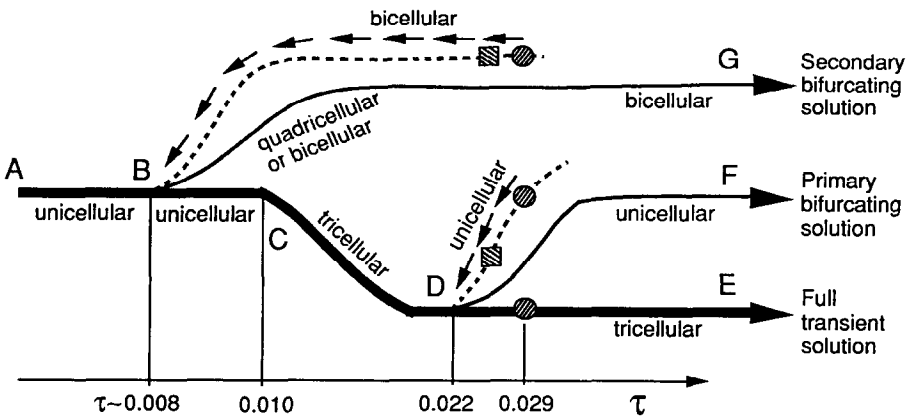

FIG. 4. A bifurcation map for the inward melting process. The parameter values are $Ra = 1.2 \times 10^6$, $Ste = 0.133$ and $S_C = 0.004$.

appear with further increase in Ra_δ (see Fig. 7 in their work).

- No unicellular steady-state solution exists between points C and D. For a narrow annulus filled with air ($\delta \sim 0.15R_w$ and $Pr = 0.7$), Powe *et al.* [17] detected experimentally the transition from unicellular to multicellular flow as Ra_δ was increased up to $Ra_\delta \sim 4000$. Our full transient solution at $\tau = 0.011$ showed that the melt thickness at $\Theta = 0$ was about $\delta \sim 0.14R_w$, or, in terms of the effective Rayleigh number, about $Ra_\delta \sim 3300$. Despite the different Pr numbers, this value remains of the same order with the critical Ra_δ from Powe *et al.* [17].
- The unicellular steady-state solutions show up again above point D. This is mainly due to the increase in the gap width. The unicellular flow pattern has been most frequently encountered in the previous experimental investigations on the natural convection in wide annuli (e.g. Kuehn and Goldstein [18]).

Now, we are at the point of disclosing the reason why the full transient solution fails to simulate the flow transition (from tricellular to unicellular) at moderate melting with high Ra. In obtaining the full transient solution, the converged tricellular solution (e.g. point D in Fig. 4) was consecutively used as the starting solution for the next time step, in a loop style. Since the final converged solution to natural convection problems depends primarily on its starting solution, the tricellular flow pattern was forced to be preserved up to near complete melting (no matter whether or not the converged solution went beyond its physical reality). However, it should be emphasized that the initial transition to tricellular pattern at early melting (point C in Fig. 4) occurred naturally due to the effect of a small gap. Such a transition is believed to be an inherent nature of the melting process at high Ra, and can be indirectly confirmed from the discussions of Rao *et al.* [6] and Powe *et al.* [17].

From the above results, we conclude that the mere numerical integration of the governing equations does not necessarily reflect its physical counterpart but may lead to anti-physical or artificial solutions, as is the case with the full transient solution. In the next subsection, we present two bifurcating solutions that can be ramified from the full transient solution. Although the bifurcating solutions introduced below may require further refinement, it is found that they are physically more meaningful than the full transient solution and agree much better with the available experimental results.

Bifurcating solutions

The bifurcation map shown in Fig. 4 reveals that there can exist two bifurcation times; one corresponds to the transition from the tricellular to unicellular flow pattern, and the other corresponds to the unicellular-to-bicellular flow transition. The exact values of these bifurcation times, $\tau_{t\,u}$ and $\tau_{u\text{-}b}$, were not accurately determined due to slow convergence but located within an uncertainty interval of $\Delta\tau = 0.001$. Such a slow convergence near the bifurcation point was also reported elsewhere [7, 8].

Assuming that the onset of thermal instability is induced from the bifurcation point, the *primary bifurcating solution* is defined to initiate from point D in Fig. 4. When $\tau = \tau_{t\,u}$ is reached, the field variables from the full transient solution are completely discarded and replaced by those from the unicellular steady-state solution. Then, the typical computation subject to our formulation is resumed thereafter. (Such a manipulation represents a numerical imitation of the flow transition, although the actual transition of the flow pattern would proceed gradually over a period of time.) Though started from the same point, the primary bifurcating solution, with its altered temperature distribution, begins to deviate from the path that would be followed otherwise. Accordingly, the primary bifurcation solution is schematically represented by a thin solid line in Fig. 4. In a similar manner, the *secondary bifurcating solution* is also introduced from the moment of $\tau = \tau_{u\,b}$.

An example of the primary and secondary bifurcating solutions as well as the full transient solution is shown in Fig. 5 for the case of $Ra = 3.6 \times 10^5$, $Ste = 0.045$ and $S_C = 0.004$. It is readily observable that the full transient solution transits to unicellular near the completion of melting (at $\tau = 0.09$). Note that this large-time solution has never been presented in the earlier studies [1–3]. It can be seen that the primary bifurcating solution results in a quite streamlined shape as melting continues. This is well consistent with the experimental data of Ho and Viskanta [3]. Also, Rieger *et al.* [2] reported that both at $Ra \cong 10^5$ and at $Ra \cong 10^6$ the secondary vortex circulation occurred in the lower melt region, which is again in accord with our primary bifurcating solution. Of further interest is that the numerical and experimental results of Saitoh and Hirose [1] agree qualitatively with our secondary bifurcating solution.

Effects of Ra and S_C on bifurcation phenomenon

The bifurcating solutions are also obtained for $Ra = 1.2 \times 10^6$, $Ste = 0.133$ and $S_C = 0.004$. For this case, Fig. 6 exhibits the timewise progression of the fluid flow and temperature distribution corresponding to both the full transient and two bifurcating solutions. The primary bifurcating solution at high Ra is qualitatively similar to that shown in Fig. 5.

As the Rayleigh number decreases, the time at which the bifurcating solutions occur is delayed because of the decrease in the effective Rayleigh number. However, there should exist a critical Ra below which no bifurcation solutions are possible at all. For example, in an extreme case of $Ra \to 0$, the fluid motion completely ceases and thus no bifurcation will take place. Actually, for a very small Ra (e.g. $Ra = 1 \times 10^3$, $Ste = 0.045$ and $S_C = 0.004$; since this small Ra case is out of the practical range of the thermal energy storage system, presentation of the

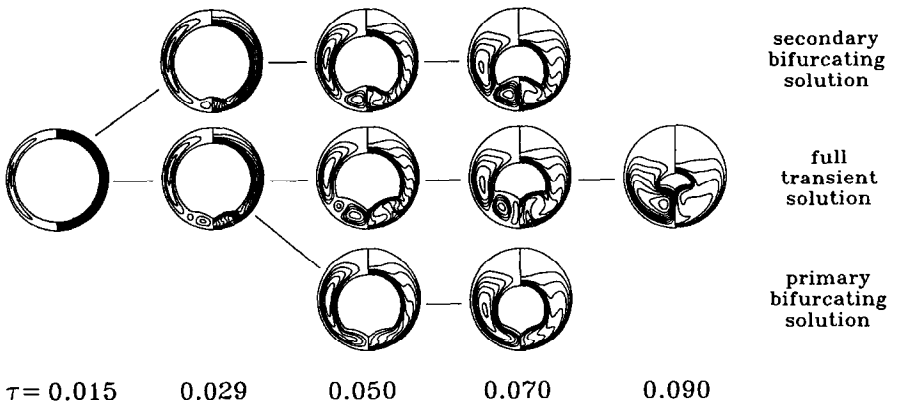

FIG. 5. The full transient solution and two bifurcating solutions for the case of $Ra = 3.6 \times 10^5$, $Ste = 0.045$ and $S_C = 0.004$. The bifurcation times are $\tau_{u-b} \sim 0.016$ and $\tau_{t-u} \sim 0.032$. The isotherm lines are drawn with equal increment of $0.1(T_w - T_f)$.

corresponding results is omitted), it was found that the fluid flow remained unicellular at all times and thus a well streamlined shape of the interface persisted up to near complete melting.

When the subcooling number alone was increased to $S_C = 0.1$ with other parameters fixed ($Ra = 1.2 \times 10^6$ and $Ste = 0.133$), the primary bifurcating solution started at $\tau_{t-u} \sim 0.026$. This is because the presence of subcooling impedes the development of natural convection, thereby delaying the onset of thermal instability. Since many of the features associated with the subcooling closely resemble the preceding results, further discussion regarding the subcooling effect is omitted here.

Comparison with the available experimental data

Figure 7 displays the interface locations at $\tau = 0.011$, 0.021 and 0.055 for the case of $Ra = 1.2 \times 10^6$, $Ste = 0.133$ and $S_C = 0.004$. The solid lines represent the available experimental data that were obtained by Ho and Viskanta [3] under nearly the same situation specified above. As can be expected, the interface location from the primary bifurcating solution agrees much better with the experiment than does the full transient solution. The experimental results clearly show the *pear-like* shape of the solid core at $\tau = 0.055$, which is a consequence of the flow transition mentioned earlier. Under a similar experimental circumstance ($Ra \cong 10^6$ and $Ste \cong 0.1$), Rieger *et al.* [2] also reported a pear-like but a little more blunted shape at $\tau = 0.05$. Emphasis is laid here on the fact that the reliability of prediction should be appraised by the interface location (rather than the melt volume fraction) [3].

Figure 8 presents another assessment of our prediction against the available experimental data [3] in terms of the melt volume fraction. To quantify the significance of the natural convection relative to conduction, pure conduction solutions (i.e. with $Ra = 0$) are also presented in Fig. 8. In general, the predicted melting rate agrees well with the experimental data at $Ra = 3.6 \times 10^5$. However, at high Ra, both the transient and bifurcating solutions considerably overestimate the data during the convection-dominated

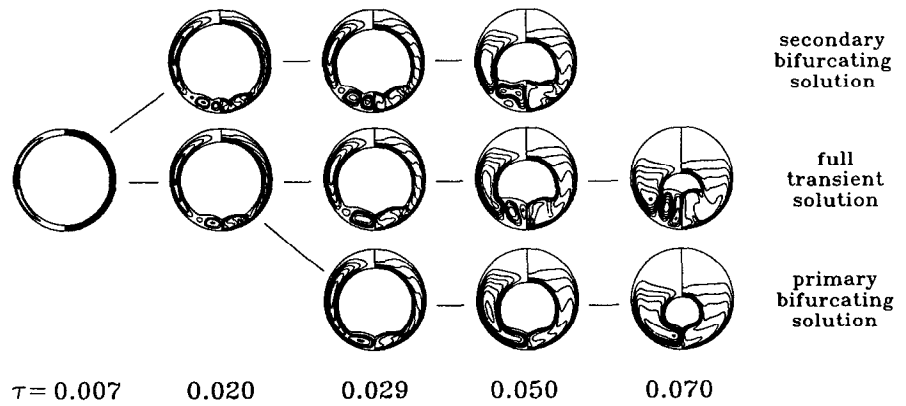

FIG. 6. The full transient solution and two bifurcating solutions for the case of $Ra = 1.2 \times 10^6$, $Ste = 0.133$ and $S_C = 0.004$. The bifurcation times are $\tau_{u-b} \sim 0.008$ and $\tau_{t-u} \sim 0.022$.

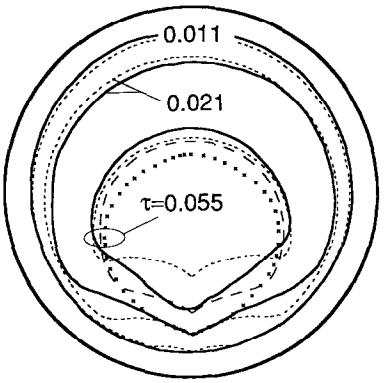

FIG. 7. The loci of the melting fronts for $Ra = 1.2 \times 10^6$, $Ste = 0.133$ and $S_C = 0.004$. Ho and Viskanta [3]: experiment (solid lines) and simulation (cross symbols). The present study: the full transient solution (dotted lines) and the primary bifurcating solution (dashed line).

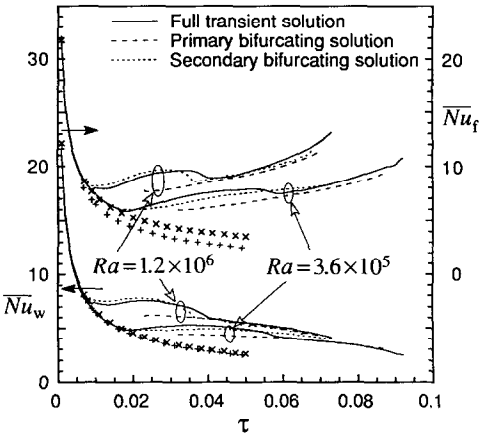

FIG. 9. The temporal variation of the average heat transfer coefficients. See Fig. 7 for legends.

stage. Especially, it can be noted that the primary bifurcating solution is closer to the data at $Ra = 1.2 \times 10^6$ than other solutions.

The occurrence of bifurcation has a great influence on the heat transfer characteristics during melting, due to the different flow structures. Figure 9 shows the timewise variation of the average Nusselt numbers evaluated from

$$\overline{Nu}_f = \frac{1}{l_f(\tau)} \int \frac{\partial \theta}{\partial n} dl_f \quad \text{and} \quad \overline{Nu}_w = \frac{1}{l} \int \frac{\partial \theta}{\partial n} dl \quad (14)$$

where $l_f(\tau)$ and l represent the circumferences of the interface and the cylinder wall, respectively; and n is normal to the integration path. One thing worthy of special remark is the variation mode of $\overline{Nu}_f$. Our full transient solution, regardless of its physical reality at late melting, indicates that $\overline{Nu}_f$ varies smoothly with time even at high Ra. However, Rieger *et al.* [2] claimed that it underwent an oscillatory variation at late melting with high Ra. Furthermore, they asserted that at $Ra \cong 10^6$ a surprisingly rapid evolution of the flow pattern was predicted with a coarse 21×31 grid system (cf. Fig. 11 in their work). To explain this unusual behavior, they postulated that the thermodynamic instability due to three-dimensional effect was responsible for such an erratic motion and also for the oscillatory variation of $\overline{Nu}_f$, although their numerical formulation was restricted to the two-dimensional case. In their work, no explicit discussion was made on whether their solutions obeyed the energy conservation principles to within an acceptable tolerance, and on whether their mesh velocities were discretized in consistence with the geometric conservation law the failure of which might trigger the oscillation and instability problems [19]. Furthermore, their numerical treatment was based on the central difference approximations that might be encountered with the stability problem at high Ra.

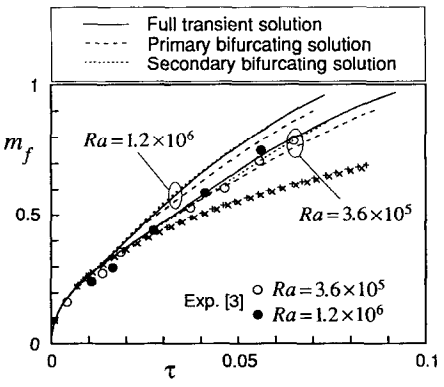

FIG. 8. The timewise variation of the melt volume fraction with $S_C = 0.004$ for two cases; one for $Ra = 1.2 \times 10^6$ and $Ste = 0.133$; and the other for $Ra = 3.6 \times 10^5$ and $Ste = 0.045$. Pure conduction solutions for $Ste = 0.133$ (cross symbol) and for $Ste = 0.045$ (plus symbol).

The discontinuities in both $\overline{Nu}_f$ and $\overline{Nu}_w$ curves at the onset of tricellular to unicellular bifurcation are mainly due to the effect of spontaneous flow transition which is numerically imitated here. In order to simulate the flow transition in a more sophisticated way, it may be required to impose a small amount of disturbances to the field variables and continue computation. However, we expect that even when the flow transition is allowed to occur in a period of time, the subsequent outcome will agree, at least qualitatively, with the present results.

SUMMARY

The inward melting process in a horizontal cylinder was re-examined here to explain the perplexing discord between the existing studies. Our preliminary results showed that the full transient solution from the model equations could lead to anti-physical solutions especially at late melting stage.

In order to establish more meaningful solutions to the inward melting process, a bifurcation map was

first drawn by examining whether or not there existed a multiple number of steady-state natural convection solutions for a series of geometric configurations (recorded from the full transient solution). Assuming the onset of thermal instability at the determined bifurcation points, two families of bifurcating solutions were introduced. As far as the shape of the melting surface in the lower melt region was concerned, the primary bifurcating solution was consistent with the convex pear-like appearance of the unmelted solid core, whereas the secondary bifurcating solution was associated with the concave shape. Due to the existence of these bifurcating solutions, the apparently conflicting melting patterns reported in the literature were considered to be all physically possible. It was also found that the onset of bifurcating solutions was initiated earlier as Ra increased and as the initial subcooling of the solid phase decreased.

A more realistic simulation of the present problem would call for a three-dimensional analysis in order to properly account for the flow transition due to the thermal instability of three-dimensional nature.

Acknowledgements—The present work was sponsored by the Korean Science and Engineering Foundation (KOSEF) and partially supported by the Turbo and Power Machinery Research Center. The assistance of Mr J.-S. Suh in preparation of figures is appreciated.

REFERENCES

1. T. Saitoh and K. Hirose, High Rayleigh number solutions to problems of latent heat thermal energy storage in a horizontal cylinder capsule, *J. Heat Transfer* **104,** 545–553 (1982).
2. H. Rieger, U. Projahn, M. Bareiss and H. Beer, Heat transfer during melting inside a horizontal tube, *J. Heat Transfer* **105,** 226–234 (1983).
3. C. J. Ho and R. Viskanta, Heat transfer during inward melting in a horizontal tube, *Int. J. Heat Mass Transfer* **27,** 705–716 (1984).
4. E. M. Sparrow and G. T. Geiger, Melting in a horizontal tube with the solid either constrained or free to fall under gravity, *Int. J. Heat Mass Transfer* **29,** 1007–1019 (1986).
5. T. Hirata and K. Nishida, An analysis of heat transfer using equivalent thermal conductivity of liquid phase during melting inside an isothermally heated horizontal cylinder, *Int. J. Heat Mass Transfer* **32,** 1663–1670 (1989).
6. Y. F. Rao, Y. Miki, K. Fukuda, Y. Takata and S. Hasegawa, Flow patterns of natural convection in horizontal cylindrical annuli, *Int. J. Heat Mass Transfer* **28,** 705–714 (1985).
7. A. Cheddadi, J. P. Caltagirone, A. Mojtabi and K. Vafai, Free two-dimensional convective bifurcation in a horizontal annulus, *J. Heat Transfer* **114,** 99–106 (1992).
8. Y. F. Rao, K. Fukuda and S. Hasegawa, Steady and transient analyses of natural convection in a horizontal porous annulus with the Galerkin method, *J. Heat Transfer* **109,** 919–927 (1987).
9. J. P. Caltagirone, M. Combarnous and A. Mojtabi, Natural convection between concentric spheres: transition towards a multicellular flow, *Numer. Heat Transfer* **3,** 107–114 (1980).
10. D. K. Choi and D. H. Choi, Dual solution for mixed convection in a horizontal tube under circumferentially non-uniform heating, *Int. J. Heat Mass Transfer* **35,** 2053–2056 (1992).
11. R. Krishnamurti, On the transition to turbulent convection, *J. Fluid Mech.* **42,** 295–307 (1970).
12. R. Krishnamurti, Some further studies on the transition to turbulent convection, *J. Fluid Mech.* **60,** 285–303 (1973).
13. C. E. Park and K.-S. Chang, Bifurcating solutions of inward melting in a horizontal tube. In *Transport Phenomena in Heat and Mass Transfer* (Edited by J. A. Reizes), pp. 704–714 (1992).
14. C.-J. Kim and M. Kaviany, A numerical method for phase-change problems with convection and diffusion, *Int. J. Heat Mass Transfer* **35,** 457–467 (1992).
15. C.-J. Kim, S. T. Ro and J. S. Lee, An efficient computational technique to solve the moving boundary problems in the axisymmetric geometries, *Int. J. Heat Mass Transfer* **36,** 3759–3764 (1993).
16. C.-J. Kim and M. Kaviany, A fully implicit method for diffusion-controlled solidification of binary alloys, *Int. J. Heat Mass Transfer* **35,** 1143–1154 (1992).
17. R. E. Powe, C. T. Carley and E. H. Bishop, Free convective flow patterns in cylindrical annuli, *J. Heat Transfer* **91,** 310–314 (1969).
18. T. H. Kuehn and R. J. Goldstein, An experimental and theoretical study of natural convection in the annulus between horizontal concentric cylinders, *J. Fluid Mech.* **74,** 695–719 (1976).
19. P. D. Thomas and C. K. Lombard, Geometric conservation law and its application to flow computations on moving grids, *AIAA J.* **17,** 1030–1037 (1979).